Supporting Information

Tetragonality induced superconductivity in anti-$ThCr_2Si_2$-type RE_2O_2Bi (*RE* = rare earth) with Bi square net

Ryosuke Sei,[a,b] Hideyuki Kawasoko,[a] Kota Matsumoto,[a] Masato Arimitsu,[a] Kyohei Terakado,[a] Daichi Oka,[a] Shintaro Fukuda,[a] Noriaki Kimura,[c] Hidetaka Kasai,[d] Eiji Nishibori,[d] Kenji Ohoyama,[e] Akinori Hoshikawa,[f] Toru Ishigaki,[f] Tetsuya Hasegawa,[b] and Tomoteru Fukumura*[a,g]

[a]Department of Chemistry, Graduate School of Science, Tohoku University, Sendai 980-8578, Japan.

[b]Department of Chemistry, Graduate School of Science, The University of Tokyo, Tokyo 113-0033, Japan.

[c]Department of Physics, Graduate School of Science; Center for Low Temperature Science, Tohoku University, Sendai 980-8578, Japan.

[d]Division of Physics and Tsukuba Research Center for Energy Materials Science, Faculty of Pure and Applied Sciences, University of Tsukuba, Tsukuba, 305-8571, Japan.

[e]Graduate School of Science and Engineering, Ibaraki University, Tokai 319-1106, Japan.

[f]Frontier Research Center for Applied Atomic Sciences, Ibaraki University, Tokai, 319-1106, Japan.

[g]Advanced Institute for Materials Research and Core Research Cluster, Tohoku University, Sendai, 980-8577, Japan.

* tomoteru.fukumura.e4@tohoku.ac.jp

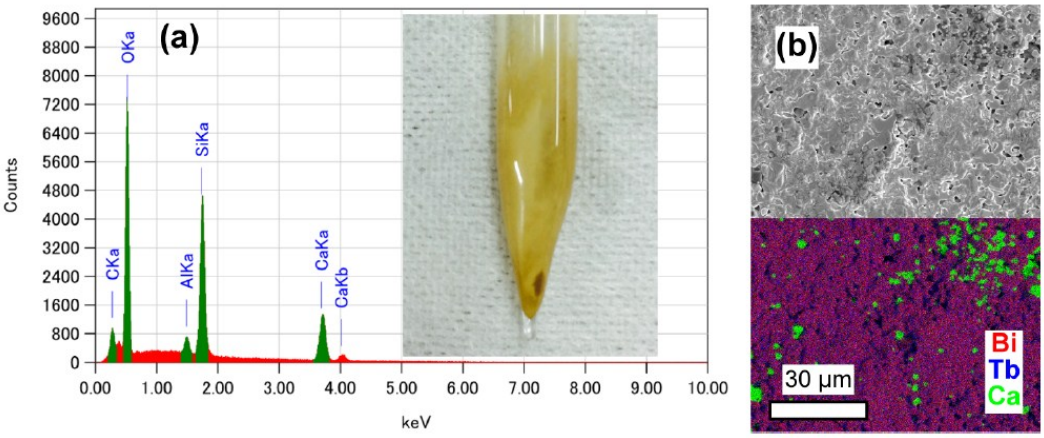

Fig. S1 (a) EDX spectrum of the quartz tube after synthesis of excess-oxygen-incorporated Tb_2O_2Bi with CaO. Inset shows a photo of the quartz tube. (b) SEM image (top) and EDX mapping (bottom) of excess-oxygen-incorporated Tb_2O_2Bi.

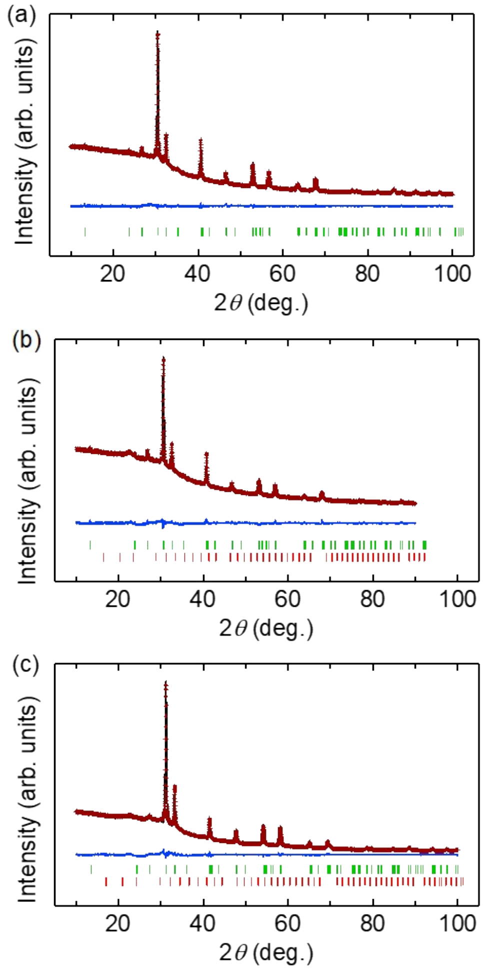

Fig. S2 X-ray diffraction patterns of the sample with the nominal composition of (a) $Tb_2O_{1.6}Bi_{1.4}$, (b) $Dy_2O_{1.4}Bi_{1.6}$, and (b) $Lu_2O_{1.3}Bi_{1.7}$ for resistivity measurement in PPMS. Brown, black, and blue curves denote measurement data, simulation pattern, and their difference, respectively. Green and red bars denote the diffraction positions of RE_2O_2Bi and RE_2O_3 phases, respectively.

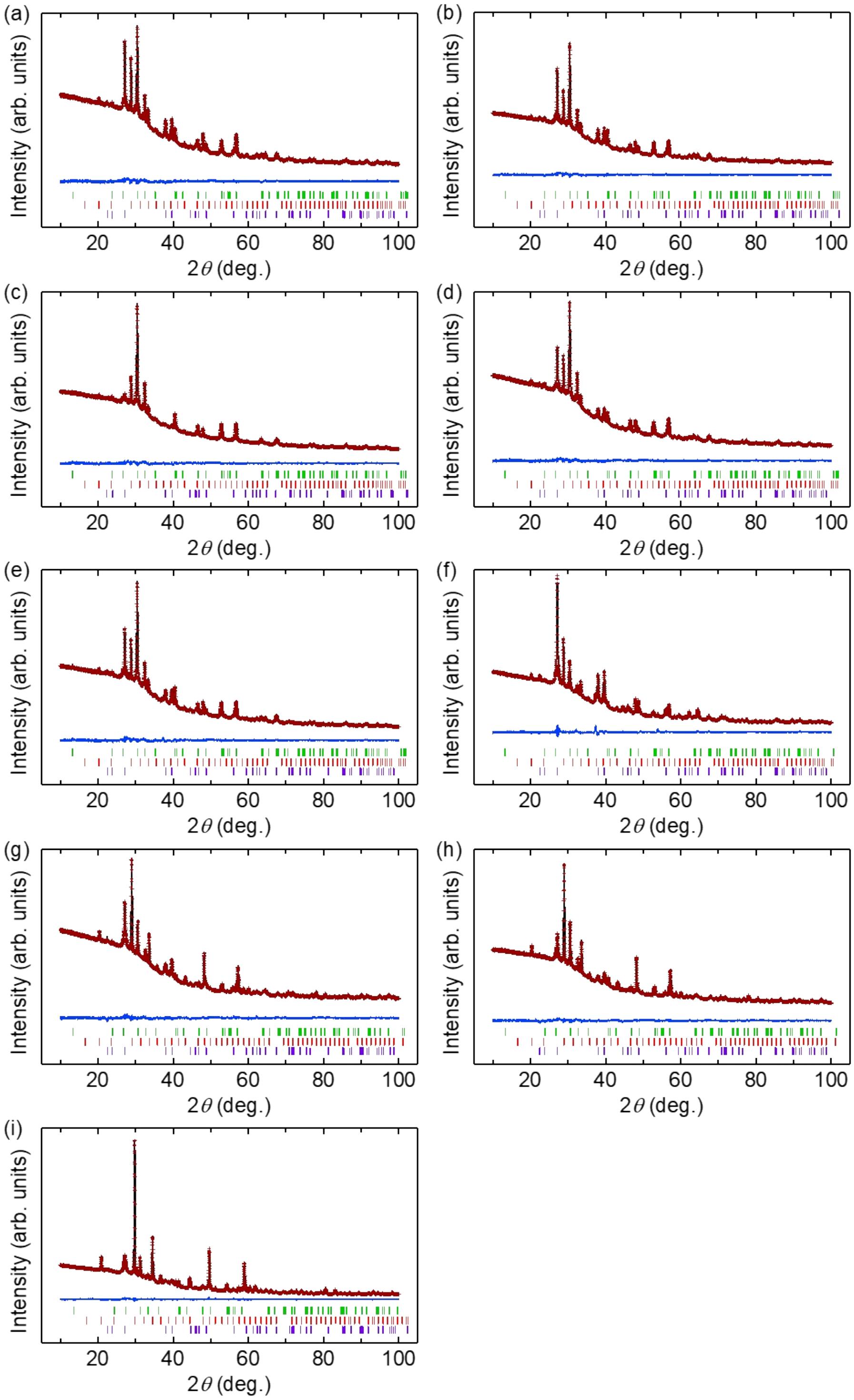

Fig. S3 X-ray diffraction patterns of the sample with the nominal composition of (a) $Tb_2O_{1.8}Bi_{1.4}$ + $(CaO)_{0.2}$, (b) $Tb_2O_{1.6}Bi_{1.6}$ + $(CaO)_{0.2}$, (c) $Tb_2O_{1.8}Bi_{1.4}$ +$(CaO)_{0.4}$, (d) $Tb_2O_{1.6}Bi_{1.4}$ + $(CaO)_{0.4}$, (e) $Tb_2O_{1.6}Bi_{1.4}$ + $(CaO)_{0.6}$, (f) $Tb_2O_{1.2}Bi_{2.0}$ +$(CaO)_{2.0}$, (g) $Dy_2O_{2.0}Bi_{1.2}$ + $(CaO)_{0.5}$, (h) $Dy_2O_{2.0}Bi_{1.0}$ + $(CaO)_{0.5}$, and (i) $Lu_2O_{2.0}Bi_{1.0}$ + $(CaO)_{0.5}$ for resistivity measurement in PPMS. Brown, black, and blue curves denote measurement data, simulation pattern, and their difference, respectively. Green, red, purple bars denote the diffraction positions of RE_2O_2Bi, RE_2O_3, and Bi phases, respectively.

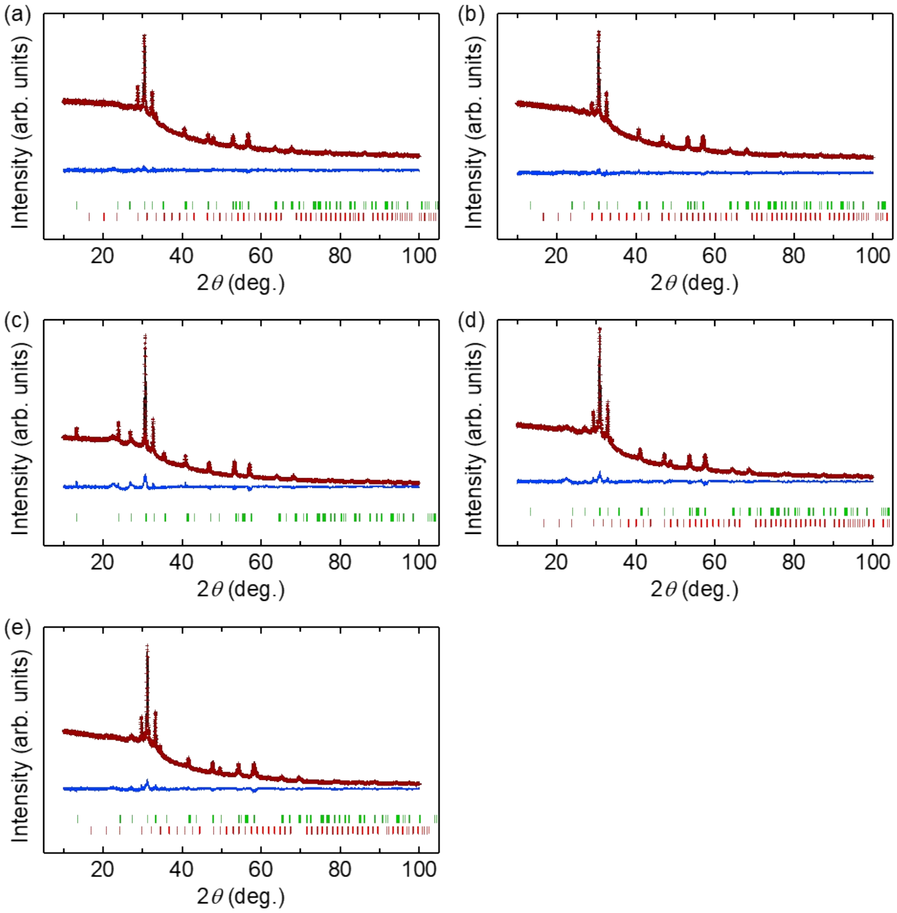

Fig. S4 X-ray diffraction patterns of the sample with the nominal composition of (a) $Tb_2O_{1.6}Bi_{1.4}$, (b) $Dy_2O_{1.4}Bi_{1.6}$, (c) $Y_2O_{1.3}Bi_{1.3}$, (d) $Er_2O_{1.4}Bi_{1.6}$, and (e) $Lu_2O_{1.3}Bi_{1.7}$ for resistivity measurement in a dilution refrigerator. Brown, black, and blue curves denote measurement data, simulation pattern, and their difference, respectively. Green and red bars denote the diffraction positions of RE_2O_2Bi and RE_2O_3 phases, respectively.

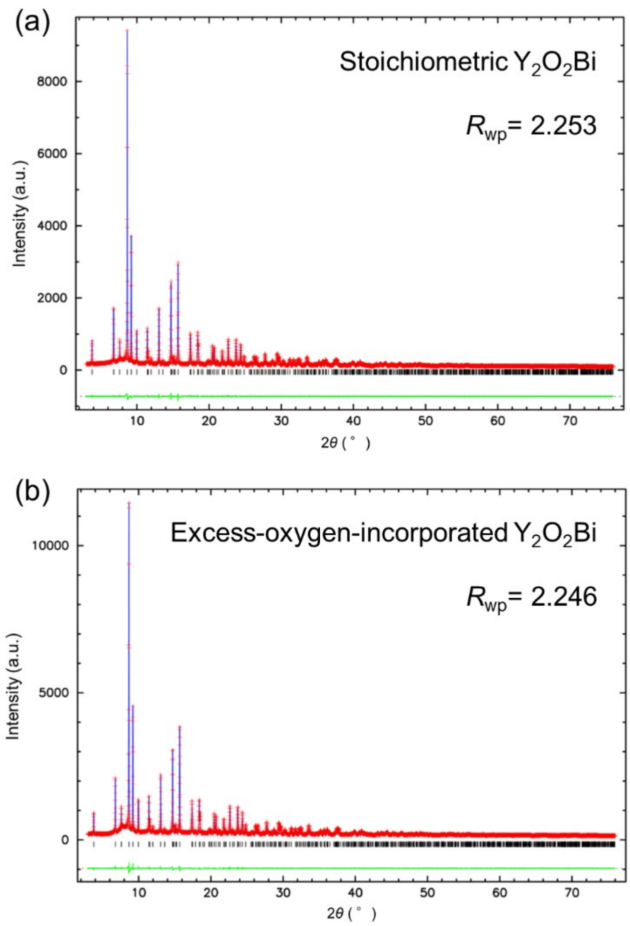

Fig. S5 Synchrotron X-ray diffraction patterns and fitting results of Rietveld refinements for (a) stoichiometric and (b) excess-oxygen-incorporated Y_2O_2Bi samples. Red, blue, and green curves denote measurement data, simulation pattern, and their difference, respectively. Black bars indicate the diffraction positions of Y_2O_2Bi phases (R_{wp}: R-factor).

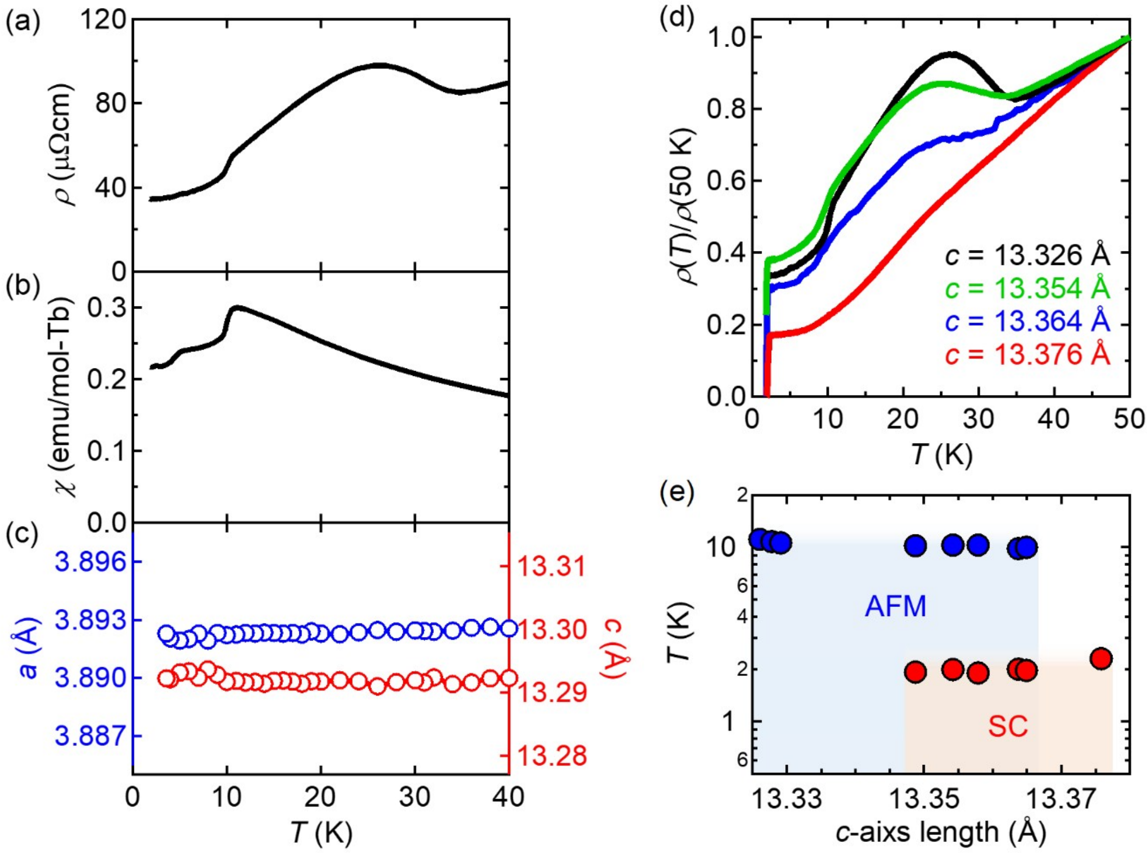

Fig. S6 Temperature dependence of (a) resistivity, (b) magnetic susceptibility, and (c) *a*- and *c*- axis lengths for stoichiometric Tb_2O_2Bi. Standard deviations of *a*- and *c*- axis lengths were within the marker size in (c). (d) Temperature dependence of normalized resistivity for Tb_2O_2Bi with various amounts of oxygen. (e) Phase diagram of Tb_2O_2Bi as a function of *c*-axis length. Magnetic susceptibility was measured for the same Tb_2O_2B sample in Ref. 1.

Figs. S6a and S6b show the temperature dependence of resistivity and magnetic susceptibility, that was measured by a magnetometer (MPMS, Quantum Design), at low temperatures for stoichiometric Tb_2O_2Bi with c = 13.326 Å. From the resistivity measurements, three anomalies were observed at 11 K, 28 K, and 35 K. From the magnetic susceptibility and neutron diffraction measurements,[1] a kink at T = 11.1 K corresponded to antiferromagnetic ordering, indicating that the anomaly in resistivity at 11 K could be attributed to the suppression of magnetic scattering (Fig. S6a). Because of no structural phase transition below 40 K (Fig. S6c), the anomalies at 28 K and 35 K could be attributed to the crystal-field effect and the Kondo scattering, respectively, as was discussed in the heavy fermion systems such as $CeIn_3$.[2] These behaviors of stoichiometric Tb_2O_2Bi clearly indicated a correlation between conduction carriers in Bi square net and magnetic ordering in Tb_2O_2 layer. With increasing *c*-axis length from 13.345 Å to 13.365 Å, the anomaly at 11 K was slightly suppressed, followed by the emergence of superconductivity below 2.2 K, suggesting the competition between superconductivity and magnetism (Figs. S6d and S6e). In Tb_2O_2Bi with c = 13.376 Å, only superconducting transition was observed below 2.2 K without antiferromagnetic transition.

Table S1 Crystal structural data and superconducting transition temperature (T_c^{onset}) of stoichiometric RE_2O_2Bi samples for resistivity measurement in PPMS (RE = Tb, Dy, and Lu; R_{wp}: R-factor, R_e: expected R-factor, S: goodness-of-fit indicator).

Nominal composition	$Tb_2O_{1.6}Bi_{1.4}$	$Dy_2O_{1.4}Bi_{1.6}$	$Lu_2O_{1.3}Bi_{1.7}$
a (Å)	3.8997(2)	3.8813(1)	3.8077(3)
c (Å)	13.3261(7)	13.2667(3)	13.0560(9)
V (Å^3)	202.66(2)	199.85(1)	189.29(3)
RE z	0.3290(2)	0.3323(3)	0.3294(3)
R_{wp}	1.465	1.826	2.645
R_e	0.981	0.944	1.097
S	1.4939	1.9337	2.4108
RE−O (Å)	2.216	2.227	2.168
c/a	3.4172(3)	3.4181(1)	3.4289(3)
T_c^{onset} (K)	–	–	–
RE_2O_2Bi (mol%)	> 99	97.5	98.7
RE_2O_3 (mol%)	–	2.5	1.3

Table S2 Crystal structural data and superconducting transition temperature (T_c^{onset}) of excess-oxygen-incorporated RE_2O_2Bi samples for resistivity measurement in PPMS (*RE* = Tb, Dy, and Lu; R_{wp}: *R*-factor, R_e: expected *R*-factor, *S*: goodness-of-fit indicator).

Nominal composition	$Tb_2O_{1.8}Bi_{1.4}$ + $(CaO)_{0.2}$	$Tb_2O_{1.6}Bi_{1.6}$ + $(CaO)_{0.2}$	$Tb_2O_{1.8}Bi_{1.4}$ + $(CaO)_{0.4}$	$Tb_2O_{1.6}Bi_{1.4}$ + $(CaO)_{0.4}$	$Tb_2O_{1.6}Bi_{1.4}$ + $(CaO)_{0.6}$	$Tb_2O_{1.2}Bi_{2.0}$ + $(CaO)_{2.0}$	$Dy_2O_{2.0}Bi_{1.2}$ + $(CaO)_{0.5}$	$Dy_2O_{2.0}Bi_{1.0}$ + $(CaO)_{0.5}$	$Lu_2O_{2.0}Bi_{1.0}$ + $(CaO)_{0.5}$
a (Å)	3.8992(4)	3.8997(4)	3.8991(5)	3.8996(5)	3.8994(4)	3.8987(4)	3.8807(3)	3.8791(3)	3.8061(3)
c (Å)	13.3488(13)	13.3542(13)	13.3579(17)	13.3638(15)	13.3649(15)	13.376(2)	13.3035(15)	13.2990(11)	13.0633(7)
V ($Å^3$)	202.95(3)	203.09(3)	203.08(4)	203.22(4)	203.22(4)	203.31(5)	200.35(3)	200.11(3)	189.24(2)
RE z	0.3272(4)	0.3286(3)	0.3279(4)	0.3285(5)	0.3275(3)	0.3221(5)	0.3222(4)	0.3273(7)	0.3251(4)
R_{wp}	1.253	1.241	1.297	1.191	1.281	2.03	1.307	1.193	1.947
R_e	0.827	0.997	0.814	0.853	0.833	0.872	0.826	0.79	0.941
S	1.5152	1.4952	1.5942	1.3968	1.5381	2.3086	1.5818	1.5092	2.0677
RE−O (Å)	2.205	2.214	2.210	2.214	2.208	2.175	2.165	2.195	2.141
c/*a*	3.4235(5)	3.4244(5)	3.4259(6)	3.4270(6)	3.4274(5)	3.4309(6)	3.4281(5)	3.4284(4)	3.4322(3)
T_c^{onset} (K)	1.92	1.99	1.9	2.02	1.96	2.29	2.1	2.09	2.29
RE_2O_2Bi (mol%)	30.6	36.0	59.1	37.9	39.2	8.3	10.1	15.9	6.5
RE_2O_3 (mol%)	28.5	22.9	26.5	24.0	25.8	20.8	46.3	54.4	64.8
Bi (mol%)	40.9	41.1	14.4	38.0	35.0	70.9	43.7	29.7	28.6

Table S3 Crystal structural data and superconducting transition temperature (T_c^{onset}) of stoichiometric RE_2O_2Bi samples for resistivity measurement in a dilution refrigerator (RE = Tb, Dy, Y, Er, and Lu; R_{wp}: R-factor, R_e: expected R-factor, S: goodness-of-fit indicator).

Nominal composition	$Tb_2O_{1.6}Bi_{1.4}$	$Dy_2O_{1.4}Bi_{1.6}$	$Y_2O_{1.3}Bi_{1.3}$	$Er_2O_{1.4}Bi_{1.6}$	$Lu_2O_{1.3}Bi_{1.7}$
a (Å)	3.8990(2)	3.88093(12)	3.8744(2)	3.84833(14)	3.80688(12)
c (Å)	13.3253(8)	13.2696(6)	13.2468(9)	13.1743(8)	13.0211(8)
V (Å^3)	202.57(2)	199.863(13)	198.850(2)	195.11(2)	188.706(14)
RE z	0.3338(7)	0.3328(6)	0.3310(4)	0.3262(4)	0.3246(3)
R_{wp}	1.823	1.74	4.154	3.305	2.97
R_e	1.518	1.461	1.663	1.704	1.705
S	1.201	1.1909	2.4977	1.9399	1.7415
RE–O (Å)	2.247	2.230	2.215	2.170	2.137
c/a	3.4177(2)	3.4192(2)	3.4191(3)	3.4234(2)	3.4204(2)
T_c^{onset} (K)	–	–	1.50	1.31	1.26
RE_2O_2Bi (mol%)	69.9	85.1	> 99	85.1	77.5
RE_2O_3 (mol%)	30.1	14.9	–	14.9	22.5

Table S4 Crystal structural data of stoichiometric and excess-oxygen-incorporated Y_2O_2Bi samples evaluated by synchrotron X-ray diffraction measurement. (R_{wp}: R-factor).

Nominal composition	a (Å)	c (Å)	v (Å^3)	Y z	R_{wp}	RE–O (Å)	c/a	Purity (mol%)
Stoichiometric Y_2O_2Bi	3.86346(2)	13.21274(9)	197.218(2)	0.33325(4)	2.253	2.223	3.41992(3)	> 99
Excess-oxygen-incorporated Y_2O_2Bi	3.86526(2)	13.23378(9)	197.716(2)	0.33294(4)	2.246	2.223	3.42377(3)	> 99

References

1. H. Kawasoko, K. Ohoyama, R. Sei, K. Matsumoto, D. Oka, A. Hoshikawa, T. Ishigaki, T. Fukumura, *AIP Adv.* 2019*,* **9**, 115301.
2. G. Knebel, D. Braithwaite, P. C. Canfield, G. Lapertot, J. Flouquet,, *Phys. Rev. B* 2001, **65**, 024425.